International Journal of Pharmaceutics 643 (2023) 123211

Contents lists available at ScienceDirect

International Journal of Pharmaceutics

journal homepage: www.elsevier.com/locate/ijpharm

Investigating freezing-induced acidity changes in citrate buffers

Behera Susrisweta [a], Lukáš Veselý [a], Radim Štůsek [a], Astrid Hauptmann [b], Thomas Loerting [c], Dominik Heger [a,*]

[a] Department of Chemistry, Faculty of Science, Masaryk University, Kamenice 5, 625 00 Brno, Czech Republic
[b] Sandoz GmbH, 6336 Langkampfen, Austria
[c] Institute of Physical Chemistry, University of Innsbruck, Innrain 52c, 6020 Innsbruck, Austria

ARTICLE INFO

Keywords:
Stabilization
Freeze-concentrated solution
Hammett acidity function
Differential Scanning Calorimetry
Glass Transition Temperature
Cryomicroscopy
Sulfonephthalein indicators

ABSTRACT

Citrate buffers are commonly utilized in the field of biomolecule stabilization. We investigate their applicability in the frozen state within a range of initial pHs (2.5 to 8.0) and concentrations (0.02 to 0.60 M). Citrate buffer solutions subjected to various cooling and heating temperatures are examined in terms of the freezing-induced acidity changes, revealing that citrate buffers acidify upon cooling. The acidity is assessed with sulfonephthalein molecular probes frozen in the samples. Optical cryomicroscopy combined with differential scanning calorimetry was employed to investigate the causes of the observed acidity changes. The buffers partly crystallize and partly vitrify in the ice matrix; these processes influence the resulting pH and allow designing the optimal storage temperatures in the frozen state. The freezing-induced acidification apparently depends on the buffer concentration; at each pH, we suggest pertinent concentration, at which freezing causes minimal acidification.

1. Introduction

Buffers are commonly used in numerous pharmaceutical formulations to control the pH and to ensure the optimum chemical and physical stability of active pharmaceutical ingredients (Trissel et al. 1996, Kheirolomoom et al. 1999, Waterman et al. 2002). In the frozen state, however, the functioning of buffers may be disrupted by a number of freezing-induced stresses (Authelin et al. 2020), such as the fractional crystallization of the components (Murase and Franks 1989, Badawy and Hussain 2007, Sundaramurthi et al. 2010, Sundaramurthi and Suryanarayanan 2011, Heger et al. 2023), freeze concentration (Heger et al. 2005, Kasper and Friess 2011, Hauptmann et al. 2018), and the Workman-Reynold effect (Takenaka et al. 2006, Bartels-Rausch et al. 2014, Krausková et al. 2016, Imrichova et al. 2019).

Freezing embodies a vital part of the biomolecule stabilization process, it constitutes the initial step in the process of freeze-drying (lyophilization), which has gained in importance in recent years within the pharmaceutical, biochemical, and food industries (Seema Thakral et al. 2021). However, the degradation processes that accompany the freezing and lyophilization are still not understood adequately. The global pandemic of SARS-CoV-2 (COVID-19) has emphasized the necessity to comprehend low-temperature storage, the obvious reason being that COVID-19 vaccines must be stored at (ultra)low temperatures; thus, it is not surprising to observe the current struggle to stabilize the vaccines (Schoenmaker et al. 2021, Wouters et al. 2021).

Freezing comprises a complex series of events, the first stage being the growth of the ice crystals, which expulses all solutes to the ice grain boundaries; in this area, the solutes concentrate, forming a freeze-concentrated solution (FCS) in the veins also known as triple junctions (Krausko et al. 2014, Vetráková et al. 2019, Vetráková et al. 2020, Závacká et al. 2021). The prior studies have explored trivial increases in the concentration (Literak et al. 2003, Heger et al. 2006), partial crystallization of the salts, (Murase and Franks 1989, Sundaramurthi et al. 2010, Sundaramurthi and Suryanarayanan 2011a, b, Vetráková et al. 2017) and uneven incorporation of the ions into the ice lattice (Workman and Reynolds 1950, Heger et al. 2006, Krausková et al. 2016, Imrichova et al. 2019); all of these aspects can lead to an acidity change during the freezing.

Various experimental methods have been employed to study the behavior of the crystallization and pH changes in frozen buffer solutions. Such investigation includes scenarios where the pH and composition of the liquid portion of a frozen solution were determined at room temperature (RT) after the liquid phase had been physically separated from the frozen one at sub-zero temperatures (Van den Berg and Rose 1959), upon pH measurement with a low-temperature electrode (Berg 1961, Sundaramurthi and Suryanarayanan 2011a, b), and with techniques

---

* Corresponding author.
E-mail address: hegerd@chemi.muni.cz (D. Heger).

https://doi.org/10.1016/j.ijpharm.2023.123211
Received 6 June 2023; Received in revised form 4 July 2023; Accepted 5 July 2023

exploiting an in situ indicator probe to reflect a change of the proton concentration in its proximity; the indicator probes were examined either visually (Orii and Morita 1977) or by means of UV–Vis absorption spectroscopy (Krausková et al. 2016, Vetráková et al. 2017, Vesely et al. 2021). Alternatively, X-ray diffraction at sub-ambient temperatures (Cavatur and Suryanarayanan 1998), DSC (Murase and Franks 1989, Chang 1992), or NMR (Li et al. 2021) were applied to establish the acidity of the frozen samples indirectly.

Research on the phosphate buffer performed via the above-outlined techniques has exposed the unsuitability of the buffer for lyophilized formulations; such a condition arises from selective crystallization of the basic component (Na_2HPO_4) during freezing, a process that produces significant pH changes (Van den Berg and Rose 1959, Van den Berg 1966, Krausková et al. 2016, Thorat and Suryanarayanan 2019). Conversely, the citrate buffer was deemed not to crystallize during the freezing, as the DSC glass formation signatures were observed (Shalaev et al. 2002).

Citric acid finds extensive application in the food industry as not only an antioxidant and preserving agent (Laird 1997, Maltini et al. 1997, Caillet et al. 2006, Daneshfar et al. 2011) but also an excipient for the lyophilization of biopharmaceutical formulations (Summers and Enever 1976, Timko and Lordi 1979, Abbatt and Nowak 1997, Lu and Zografi 1998); such preference arises from the citrate's broad buffering range, minimal pH changes with temperature, and supposed resistance to crystallization during the freezing and lyophilization (Lu and Zografi 1997, Shalaev and Gatlin 2005, Wu et al. 2015, Nangare et al. 2021). These properties are especially useful in the stabilization of therapeutic proteins in frozen large-scale formulations (Summers and Enever 1976, Timko and Lordi 1979), including the solubilization and sustained delivery of anti-HIV (human immunodeficiency virus) drugs (Vijayarajkumar 2012); by extension, one of the domains that benefit from citrate buffers is tissue engineering (synthesis of biodegradable scaffold) (Yang et al. 2004, Thomas and Nair 2011), the reason being the production of amorphous FCSs that have a high glass transition temperature, T_g (Kets et al. 2004, Kadoya et al. 2008, Izutsu et al. 2009). Citric acid plays also an important role in the naturel environment, where its (photo)degradation is deemed to depend on the state, be it amorphous or crystalline (Ueda et al. 1995, Jung and Kawamura 2011, Chatre et al. 2019, Chang et al. 2020).

Previously, two distinct FCS_s with varied concentrations, and thus T_gs, were reported in citric acid (Webb et al. 2002, Bogdan et al. 2014a, b, Hauptmann et al. 2018). A maximally freeze-concentrated solution (FCS_1) is formed by trapping the solutes in the interdendritic spaces between the ice crystals; the process is sometimes denoted as microscopic scale cryoconcentration (Kolhe et al. 2010). In contrast, *macroscopic* scale cryoconcentration (producing FCS_2) occurs when the solutes are progressively pushed by the freezing front of the growing dendrites; thus, FCS_2 embodies the last item to vitrify in the cooling process (Bogdan et al. 2016, Bogdan and Molina 2017). Macroscopic scale cryoconcentration is very difficult to control because it depends on several parameters, for instance, the size of the sample and the temperature gradients therein (Hauptmann et al. 2019, Hauptmann et al. 2021). As FCS_1 exhibits a higher concentration than the macroscopically cryoconcentrated solution, it facilitates a glass transition at a higher temperature, typically represented as T_{g1}, similarly to the T_{g2} used in FCS_2.

Despite the importance of citrate buffers in the pharmaceutical industry, rigorous research on the crystallization behavior, acidity in the frozen state, and microstructure in the frozen solutions is still lacking. The primary aim of this study is to evaluate the freezing- and temperature-induced acidity changes in citrate buffer solutions (CBSs) and to rationalize the freezing procedure.

2. Methods

2.1. Materials

The citric acid (CAS-77–92-9) was purchased from PENTA. The sodium hydroxide (CAS 1310–73-2) (PENTA) and hydrochloric acid (CAS 7647–01-0) were purchased from LACHNER and then used to partially neutralize the acid and base to prepare the CBSs. All the chemicals were employed as received, without further purification. A pH meter, calibrated with standard buffer solutions (standard, NIST-certified buffers; pH 4.01, 7.00, and 10.00), was applied. The chemical structure of citric acid is presented in Fig. 1.

2.2. Differential scanning calorimetry (DSC)

To perform the calorimetric analysis, we used a Perkin Elmer DSC 8000 differential scanning calorimeter. Briefly, an amount of 25–30 mg of the solution was loaded into an aluminium crucible and hermetically sealed with a lid at RT. An empty aluminium pan was employed as the reference. The crucible was inserted into the DSC oven to be tempered at 20 °C for 5 min. Subsequently, it was cooled down to −100 °C at the cooling rates of 30 $°C\ min^{-1}$ (fast cooling) and 3 $°C\ min^{-1}$ (slow cooling), and then reheated to 20 °C at the rate of 30 $°C\ min^{-1}$ after a 5-minute isothermal lapse. The cooling/heating cycle was repeated three times. The DSC was calibrated by transitions in cyclopentane, cyclohexane, indium, and adamantane, with an accuracy of ± 1 °C (Hemminger and Höhne 1979). Furthermore, a sapphire was used to calibrate the latent heat and change in the heat capacity, enabling an accuracy of $\pm$ 0.1 J mol^{-1} °C.

2.3. UV–VIS spectroscopy

The acidity of both the liquid and the frozen samples was assessed with UV–VIS spectroscopy of the sulfonepthalein pH indicators. The samples were measured in plastic cuvettes sized 1 × 1 cm (Brand UV cuvettes, macro, Cat. No. 7591 70) to be investigated immediately after the cuvettes had been removed from the cooling bath. The sulfonepthalein indicators are known to reliably report the acidity also in frozen condition (Heger et al. 2006, Govindarajan et al. 2014). The measurements were executed using an Agilent DRA 2500 integrating sphere coupled to a Cary 5000 spectrophotometer; generally, the integrating sphere collects the scattered light, which is transmitted through the frozen sample. A similar procedure was employed in our previous studies (Krausková et al. 2016, Vetráková et al. 2017, Vesely et al. 2021). Although we did not control the temperature of the sample when recording the absorption spectra, no changes were observed in the spectra within the time period required for the measurement. In each experiment, we conducted triplicate measurements, reporting the average value. The standard error of the mean (SEM) was computed based on varying sample sizes (n) ranging from 12 to 15 (n = 12 for samples cooled at −40 °C and then further cooled to −196 °C while n = 15 for other cooling methods) and visually represented using error bars. Distilled water and ice made therefrom facilitated the baseline correction in the solutions and the frozen samples, respectively.

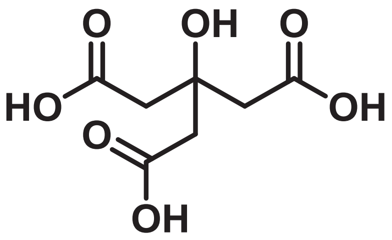

Fig. 1. The chemical structure of citric acid.

2.4. Optical cryomicroscopy (OCM) measurements

Images of the frozen buffer solutions were taken by using an optical microscope BX-51 (Olympus Corporation, Japan) combined with a temperature-controlled cryostage LTS420 (Linkam Scientific Instruments, UK). With the cryostage, temperatures down to −196 °C can be reached via liquid nitrogen as the cooling medium. A drop of the sample (approx. 0.5 µl) was placed on the object plate, positioned into the cryo-chamber, and enclosed with a cover glass to prevent condensation. Loaded at ambient temperature, the samples were frozen to −100 °C at the rates of 2 °C min^{-1}, 20 °C min^{-1}, 30 °C min^{-1}, and 40 °C min^{-1} to be analyzed isothermally by applying either unpolarized transmitted light or light transmitted through polarization filters. The attenuated polarized light is usable in visualizing the structural changes, crystal sizes, and orientation in the droplet through different intensities of the applied color. The morphology changes in the frozen form were determined with 5×, 10×, 20× and 50× objectives (Olympus Corporation, Japan) and employing the Linksys 32 software. Using this equipment, we captured relevant images and recorded videos for the analysis. The disadvantage of the method lies in accumulation of ice crystals on the top glass, especially at low cooling rates; this effect generates through the environmental humidity.

2.5. Acidity probes

Four sulfonepthalein indicators, whose general structure is shown in Fig. 2, were applied in an individual manner. Table 1 shows the positions of the atoms of the four applied indicators of the sulfonepthalein family. These indicators cover a wide pH range, approximately 0–10, as each of them can probe the pH range of p*K*a ± 1.5. The pure form of the indicators was obtained as follows: (1) For the cresol red (CR), A in 4.6 M HCl, B at pH 4.0, and C at pH 12.0; (2) for bromophenol blue (BPB), B at pH 0.8 and C at pH 7.1 (3) for the bromocresol green (BCG), B at pH 2.0 and C at pH 7.0; and (4) for the bromocresol purple (BCP), B at pH 3.0 and C at pH 9.0. The ratios of the protonated and deprotonated forms were calculated by fitting the pure forms' spectra into the measured spectrum via a MATLAB script to compute the Hammett acidity function (H_{2-}) values (Krausková et al. 2016, Vetráková et al. 2017, Vesely et al. 2021). The chemical structures of the four sulfonephthalein indicators applied in the experiment and the values of the absorption bands' maxima along with their $\mathrm{p}K_\mathrm{a}$s are shown in Figures S1, 2, 3,4 and Table S1, respectively.

2.6. Hammett acidity functions H2-frozen

Since the pH scale is used as a measure of acidity only in dilute aqueous solutions, the Hammett acidity functions $H_{2\text{-}}^{\text{frozen}}$ are employed here to quantify the acidity of the frozen solutions. In this article, $H_{2\text{-}}^{\text{frozen}}$ represents the acidity function of the fully deprotonated sulfonephthalein indicators. The notation was established to specify the protonation equilibrium of polyprotic acids in such a manner that the subscript of the *H* specifies the charge of the base in question (Govindarajan et al. 2006a). We have

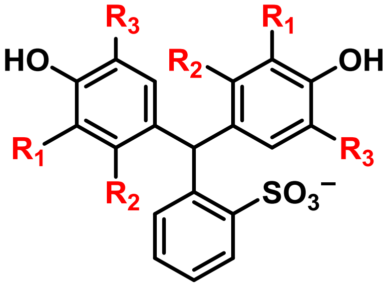

Fig. 2. The general chemical structure of the sulfonepthalein indicators.

Table 1
The molecules present at R_1, R_2, and R_3, as shown in Fig. 2 for various indicators.

Indicator	Position		
	R_1	R_2	R_3
Cresol red (CR)	CH_3	H	H
Bromophenol blue (BPB)	Br	H	Br
Bromocresol green (BCG)	Br	CH_3	Br
Bromocresol purple (BCP)	CH_3	H	Br

$$H_{2-}^{\text{frozen}} = pK_{a,\text{Ind}} + log\frac{c_{\text{Ind}^x}}{c_{\text{HInd}^{x+1}}} = -\log\left(a_{\text{H}^+}\left[\frac{\gamma_{\text{Ind}^x}}{\gamma_{\text{HInd}^{x+1}}}\right]\right)$$

where *c*, a_{H^+}, γ, and *x* stand for the concentration of the indicator, proton activity, indicator activity coefficient, and charge of the indicator's deprotonated form, respectively. The Hammett acidity function was extended to include non-aqueous solutions (Chatterjee et al. 2008, Alkhamis 2009). In dilute solutions, where the activity coefficients are close to 1, the values of the pH and $H_{2\text{-}}^{\text{frozen}}$ are equal. Where the activity coefficients do not equal 1, $H_{2\text{-}}^{\text{frozen}}$ replaces pH in accessing the acidity. As $H_{2\text{-}}^{\text{frozen}}$ depends on not only the proton activity but also the ratio of the indicator's activity coefficient, it can be indicator-specific (Govindarajan et al. 2006b, Pudipeddi et al. 2008). Thus, the $H_{2\text{-}}^{\text{frozen}}$ values could, in principle, differ from one another in various indicators. However, as the applied indicators belong to the same sulfonephthalein family, we expected an internal consistency between the applied indicators, following previous observations (Yi Yao et al. 1998, Vetráková et al. 2017). Examples of the indicators' spectra in 50 mM CBSs cooled down at −40 °C at a range of pH values are shown in Figures S13 to S15. If in an indicator only one form is detected, as displayed in Figure S13 for pH 1.8 and 2.0, the relevant $H_{2\text{-}}^{\text{frozen}}$ cannot be calculated, and the resulting value is delivered as a value 1.5 units smaller than the indicator's p*K*a supplemented with an arrow.

2.7. Sample preparation

Various concentrations of the CBSs, as shown in Table S2, were prepared by weighing an appropriate amount of the acid and dissolving it in a volumetric flask in deionized water. The solutions of the free acids were partially neutralized with sodium hydroxide to prepare buffer solutions with the desired pH values. For the spectroscopic examination, one of the acid-base indicators was added to the CBSs. The concentration of the indicator equaled 6×10^{-5} M.

The buffer solutions were frozen in poly (methyl methacrylate) cuvettes with a 1 cm path length, allowing UV–VIS measurements above 270 nm. We employed two cooling methods: shock cooling in liquid nitrogen (-196 °C), referred to as fast cooling, and cooling in an ethanol bath by dosing dry ice into ethanol to reach the required temperature; this method is termed slow cooling and was applied in a range of temperatures. Some samples were frozen by slow cooling to have their temperatures gradually lowered in the ethanol bath or liquid nitrogen. In another experiment, the samples were monitored during the warming. In all of the cases, the samples were kept at the desired temperature for 10 min before the measurement of the spectra.

3. Results

3.1. Differential scanning calorimetry

The DSC scans of 0.6 M CBSs at the pHs of 1.8, 4.0, 5.6, and 8.3 were recorded using the cooling rates of either 30 or 3 °C min^{-1}, always followed by the heating rate of 30 °C min^{-1}. The most dominant features in the cooling and the heating calorigrams are the water crystallization exotherm and the ice melting endotherm, respectively (Figure S5). In the 30 °C min^{-1} cooling scans, the water crystallization peak is wide, as typically observed at the high scanning rates (Figs. 3, S5(A), S6 and S7). The large exothermic crystallization peaks are notably broader in the buffer solutions compared to the pure water (Fig. 3). In contrast, slow cooling at 3 °C min^{-1} allows a sharp water crystallization peak (Figure S5(B)). Further, a detailed examination of the slow-cooled scans showed small peaks preceding the water crystallization ones (Fig. 4 and S8) at all of the examined pHs; such peaks are ascribed to the crystallization of the buffer components. Besides the crystallization events, two liquid-to-glass transitions (T_gs) can be observed at the examined pHs in the 30 °C min^{-1} scans (Fig. 5). Regarding the 3 °C min^{-1} cooling thermograms, the indications of the T_gs are still discernible, but their precise positions remain hidden in the drifting baseline (Figure S9). The onsets of the ice and buffer components' crystallization are listed in Table S3, together with the glass transition temperatures. The two glass-to-liquid transitions are well distinguished also in the heating calorigrams for both the fast and the slow cooling (Fig. 5 and S10, Table S3). In these calorigrams, only one broad melting endothermic peak was observed, covering the melting of both the buffer salts and the ice (Figure S11). The melting temperature was found to monotonically decrease with the concentration, as is demonstrated in Figure S12.

3.2. *Acidity assessment via the spectrophotometric method*

3.2.1. *Effect of the sample temperature*

The 50 mM CBSs for the range of pH values (3–8) were cooled down from RT to −10 °C and then gradually to −196 °C; subsequently, the solutions were warmed up to −25 °C, and, at each step, the frozen solution acidity was assessed spectrophotometrically, as reported in Fig. 6A. The differences between the acidities in the frozen state $H_{2\text{-}}^{\text{frozen}}$ and the liquid state at the RT pH are plotted in Fig. 6B. Upon freezing, the CBSs experienced an acidity increase ($H_{2\text{-}}^{\text{frozen}}$ drop) at all of the examined pHs, as is obvious at the first measured temperature, i.e., −25 °C: The acidification is below one unit for the pHs lower than 4.0 and rises progressively with increasing pH, exceeding 2.2 units of acidification at pH 8.0. According to their behavior during further cooling, the samples can be separated into two groups, namely, those that steadily acidify upon cooling (pHs 3.0 and 3.5) and those that, after reaching the $H_{2\text{-}}^{\text{frozen}}$ minimum, experience an $H_{2\text{-}}^{\text{frozen}}$ increase to −60 °C followed by a plateau upon further cooling to −196 °C (pHs 4.0 and above). The samples in the former group (pH 3.0 and 3.5) follow the $H_{2\text{-}}^{\text{frozen}}$ parabolic decreases with lowering temperature; the lowest $H_{2\text{-}}^{\text{frozen}}$ value corresponds to the lowest measured temperature of −196 °C. The $H_{2\text{-}}^{\text{frozen}}$ value decreases steadily from – 10 °C to −60 °C. Below −60 °C, the values remain essentially constant to increase again upon warming, without notable hysteresis. The sample at the initial pH of 4.0 exhibits the lowest $H_{2\text{-}}^{\text{frozen}}$ at −40 °C; the acidity function value then increases at a lower temperature. The samples with pHs 5.0 and above show an $H_{2\text{-}}^{\text{frozen}}$ minimum at −25 °C; the value rises upon further cooling down to −60 °C to stay unchanged down to −196 °C.

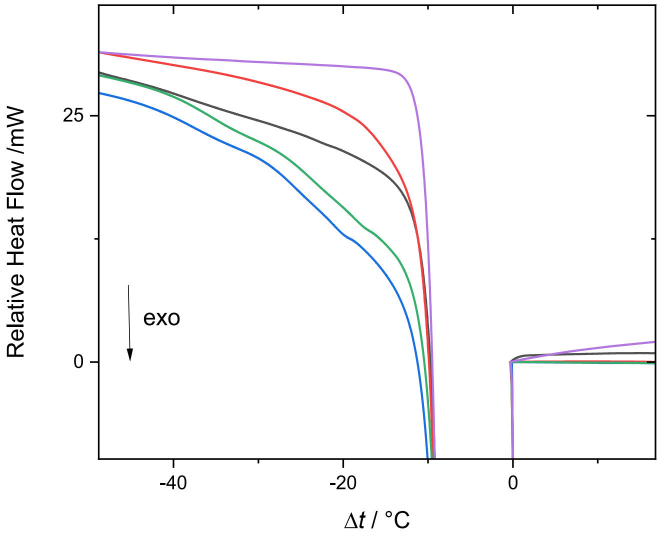

Fig. 3. The magnified DSC cooling curves of the 0.6 M CBSs, related to the pH values of 1.8 (black), 4.0 (red), 5.6 (blue), 8.3 (green), and distilled water (violet). All the thermograms are shifted to zero at the beginning of the ice crystallization to allow better comparison. The samples were cooled down from 20 °C to −100 °C at the cooling rate of 30 °C min^{-1}. The full-ranged calorigrams are shown in Figures S6 and S7. (For interpretation of the references to color in this figure legend, the reader is referred to the web version of this article.)

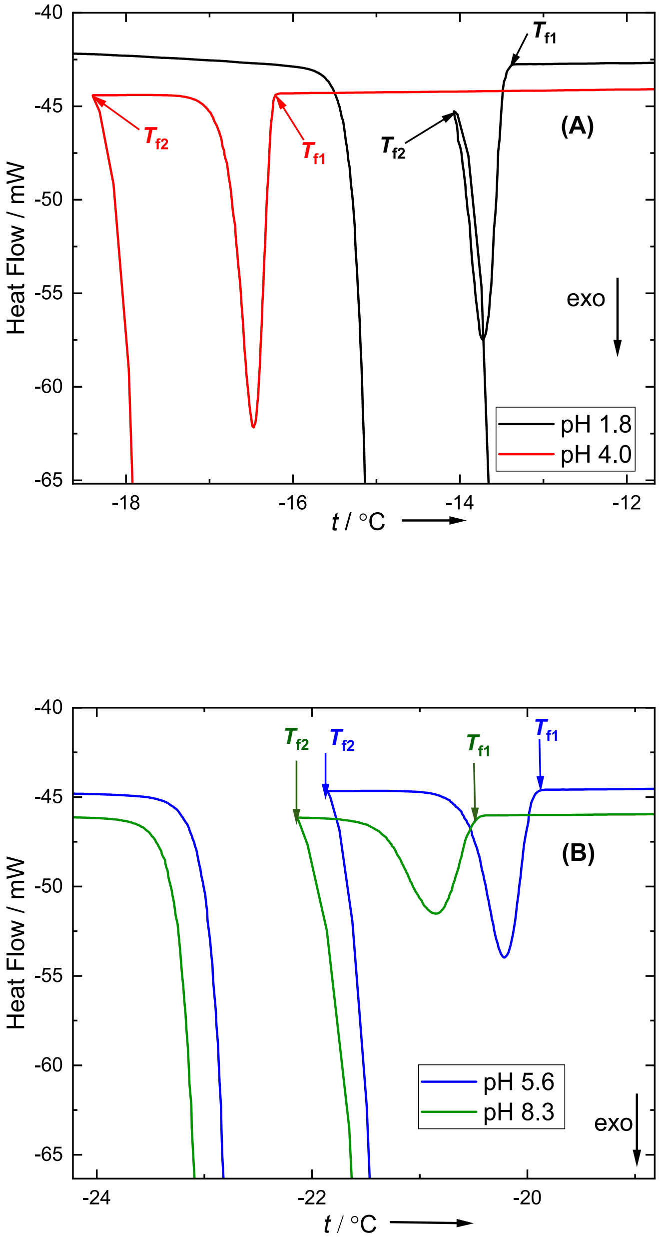

Fig. 4. The magnified DSC cooling curves of the 0.6 M CBSs, related to the pH values of 1.8 (black), 4.0 (red) (A), 5.6 (blue), and 8.3 (green) (B), color-coded in the legend. The samples were cooled down from 20 °C to −100 °C at the cooling rate of 3 °C min^{-1}. The full-ranged calorigrams are shown in Figures S8. (For interpretation of the references to color in this figure legend, the reader is referred to the web version of this article.)

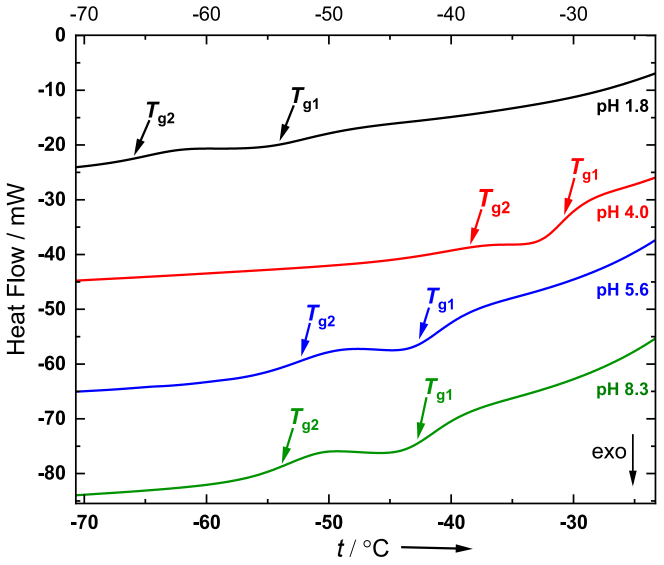

Fig. 5. The magnified DSC heating thermograms of the 0.6 M CBSs, related to the pH values of 1.8 (black), 4.0 (red), 5.6 (blue), and 8.3 (green), color-coded in the legend. The samples were cooled down from 20 °C to −100 °C, left to idle isothermally for 5 min, and finally warmed to 20 °C. Both the cooling and the heating rates were 30 °C min^{-1}. The arrows show the glass-to-liquid transitions, T_{g1}s and T_{g2}s. The values of the T_gs are given in Table S3. (For interpretation of the references to color in this figure legend, the reader is referred to the web version of this article.)

3.2.2. Cooling temperature and its impact on the freezing step through the cooling rate

The various cooling rates were applied to freeze the 50 mM CBSs in the pH range between 1.8 and 7.5. After the diverse freezing procedures, all of the samples were cooled down to −196 °C; at this temperature, the Hammett acidity (H_{2-}^{frozen}) was determined (Figure S16). The values of (H_{2-}^{frozen} - pH$^{\text{RT}}$) are represented in Fig. 7. We applied five freezing procedures: 1. immersing the sample into the boiling liquid nitrogen at −196 °C; 2. immersion into liquid methane at −196 °C (Figure S17); 3. cooling in the ethanol bath at −100 °C (Figure S18); 4. cooling in the ethanol bath at −40 °C (Figure S19); and 5. gradual cooling from −10 °C to −196 °C (Fig. 6). The trend in the acidity change at the various pHs is not substantially influenced by the manner of freezing. The smallest variation (<-1.2 units) was observed at pHs from 2.5 to 4.5 (Figure S15 to S16). The acidity, however, began to rise gradually with an increase in the initial pH, reaching ca. 2.0 units at pH 8.0 (Figure S15 and S16), and an acidification jump by more than 2.5 units was observed in the acidic solutions at pH ≤ 2.0 (Figure S13) The additional cooling down to −196 °C of the samples frozen at −40 or −100 °C did not alter the acidity markedly (Figures S18 −19).

3.2.3. Effect of the buffer concentrations

The four concentrations of the CBSs (0.020 M, 0.050 M, 0.200 M, and 0.600 M, with the mole percentages of 0.036, 0.091, 0.37, and 1.15, the pH range being 3.0 to 7.0) were frozen invariably via one of two convenient methods and then measured at four distinct temperatures. The applicable techniques lay in either fast cooling in liquid nitrogen at −196 °C or freezing at −25 °C followed by cooling down to −30 °C and −40 °C. The values averaged over the freezing methods are shown in Fig. 8, and the separated contributions are indicated in Figure S20. At pH 3.0, the concentration has only a minor influence on the resulting acidity in the frozen solution; at the higher pHs, however, a significant trend appears, as the most prominent acidification is observed at the lowest buffer concentrations. The difference in the H_{2-}^{frozen} values reaches more than 1 unit between the 0.020 M and 0.200 M solutions at the respective pHs. Having this knowledge, we tested diverse buffer concentrations to identify the optimum for freezing the buffered solutions at the pHs 4.0 to 7.0, as reported in Fig. 9; these solutions were frozen in the ethanol bath cooled with solid CO$_2$ down to the temperature of −80 °C.

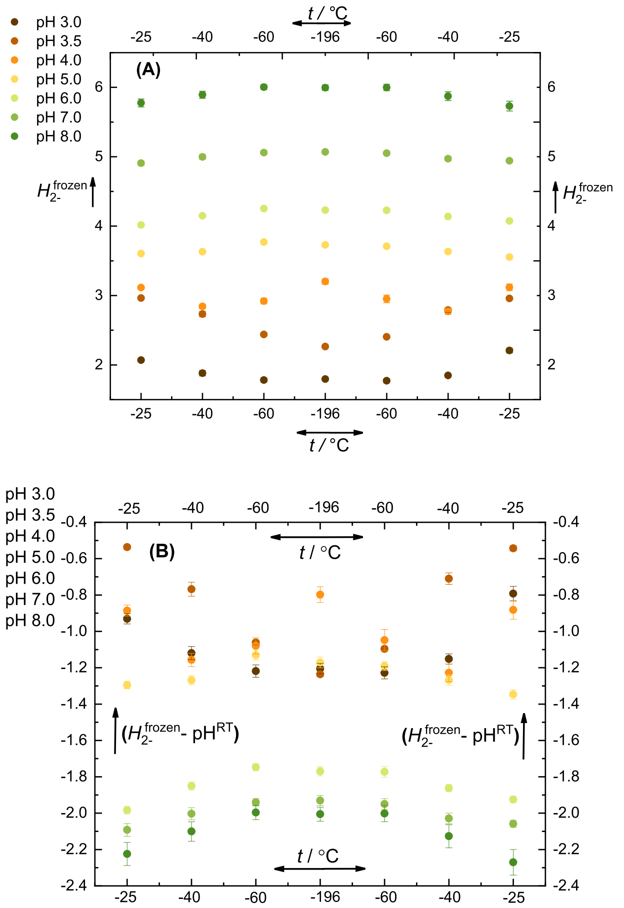

Fig. 6. (A) The Hammett acidity functions, H_{2-}^{frozen}; (B) the difference between the Hammett acidity and the initial pH$^{\text{RT}}$ values, (H_{2-}^{frozen} - pH$^{\text{RT}}$), in the solution of the frozen 50 mM CBSs at the temperatures indicated on the abscissa and at the color-coded pH values 3.0, 3.5, 4.0, 5.0, 6.0, 7.0, and 8.0. The samples were cooled down from RT to −10 °C and then gradually to − 196 °C; subsequently, the solutions were warmed up to −25 °C, and, at each step, the frozen solution's acidity was assessed spectrophotometrically, as reported. Accordingly, the plot should be read from left to right.

3.3. Optical cryomicroscopy observation

3.3.1. Impact of the cooling rate

The OCM images of single droplets of the CBSs at the pHs 1.8 (Video S1) and 4.0, the temperature being −100 °C after cooling at rates between 2 and 40 °C min^{-1}, are shown in Figs. 10, 11, and S21 (the pHs of 5.6 and 8.3 in Figures S22, S23). The images in Fig. 10 were recorded in unpolarized light, and those in Fig. 11 were acquired under polarized light to allow better observation of the individual crystallites. Further, the graphical representation in Fig. 10 exposes a frozen CBS droplet, which appears as a black circular object. Noticeable is the relatively brighter halo-like rim at the drop's periphery; this feature was found to vary with the cooling rate and the pH value of the solution (Fig. 10, 11, S22 and S23). The widest rim was observed at pH 4.0 (Fig. 10 and S21); at the other pHs, by contrast, this rim was rather modest. We infer that the translucent region is due to the non-scattering glassy FCS present in the sample. The periphery can be produced by both the FCS$_1$, interveined between the ice crystals, and the FCS$_2$, expelled out from the progressing ice. The apparent presence of the FCS on the rim of the drop

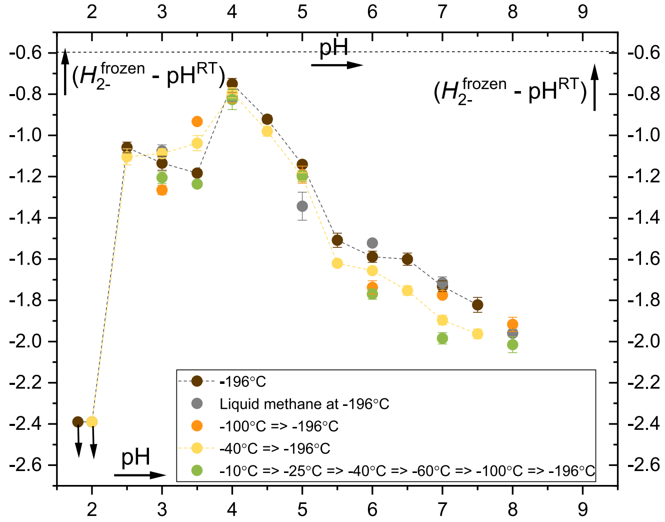

Fig. 7. The impact of the cooling rates on the difference between the Hammett acidity, H_{2-}^{frozen} (shown in Figure S16), and initial pH value (H_{2-}^{frozen} - pH^{RT}) of the original solution of 50 mM CBSs. The samples were prepared by cooling in the liquid nitrogen at −196 °C (brown), in the liquid methane at −196 °C (grey), in the ethanol bath at −100 °C (orange) or − 40 °C (yellow), or by gradual cooling down from −10 °C (green) in the liquid nitrogen (as detailed in Fig. 6). The color codes are shown in the legend. All of the samples were cooled down to −196 °C before the measurement. The CR, BCG, and BCP were employed as the indicators in the frozen samples at the pHs below 3.5, between 4.0 and 6.0, and above 6.0, respectively. The relevant lines provide visual aid. (For interpretation of the references to color in this figure legend, the reader is referred to the web version of this article.)

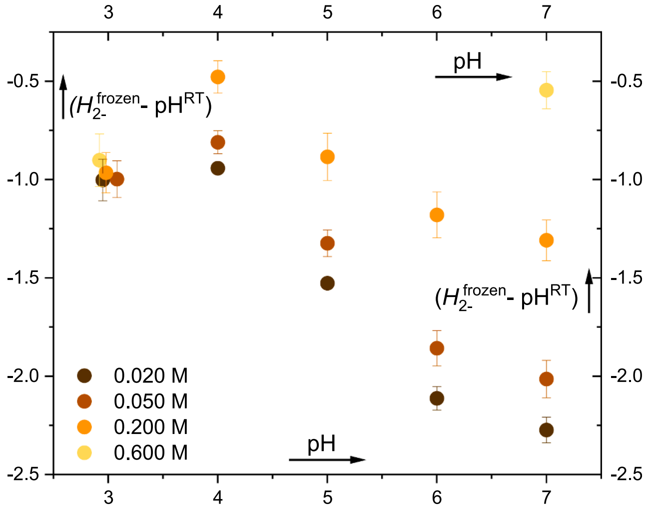

Fig. 8. The impact of the buffer concentrations 0.020 M, 0.050 M, 0.200 M, and 0.600 M, with the mole percentages of 0.036, 0.091, 0.37, and 1.15, on the difference between the Hammett acidity, H_{2-}^{frozen}, and the pH^{RT} (H_{2-}^{frozen} - pH^{RT}) of the original solutions. At each pH, the represented value is averaged over the two freezing methods and measured at the four distinct temperatures. The individual data of the experiments are shown in Figure S20; these data then allowed calculating the averages and the SEMs.

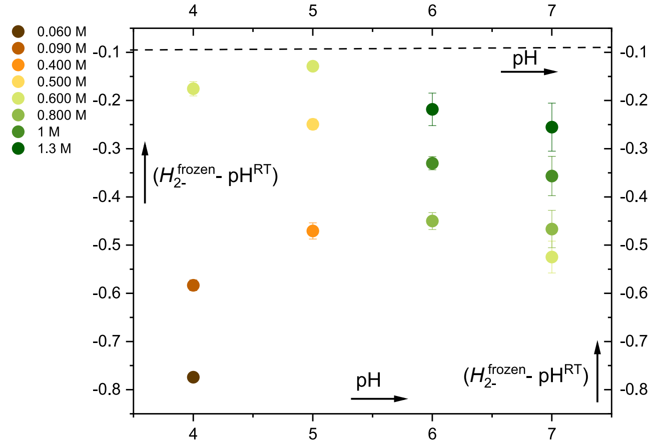

Fig. 9. The difference between the Hammett acidity, H_{2-}^{frozen}, and the original solution's pH^{RT} (H_{2-}^{frozen} - pH^{RT}), relating to both a range of pHs at RT values and the variously concentrated CBSs (color-coded in the legend). The samples were frozen in the ethanol bath with the solid CO$_2$ at the temperature of −80 °C and then measured accordingly.

is explainable by the lowest optical path length enabling the light to travel through the drop. The amount of scattered ice crystals increases towards the center of the drop, and therefore the sample looks black in the transmission light. The polarized light possesses the ability to penetrate deeper through the sample, allowing us to observe more details. In particular, the rim regions are well-resolved, including the large, oriented, needle-shaped crystals, at all of the cooling rates applied to the samples that have pH 4.0; regarding pH 1.8, this holds true only of those sample that were cooled down at 30 and 40 °C min^{-1}. The slower cooling at pH 1.8, as shown in Video S2, did not facilitate resolving the crystals, because a smooth transition of green shades was detected, suggesting an even distribution of the crystals. The black cross over the sample at pH 1.8 at 20 °C min^{-1} is an interference pattern, not important for the current study. The polarized light images allow identifying the regions where the nucleation began: For example, in the sample with pH 4.0 and cooling at 2 °C min^{-1}, the nucleation started in the upper left corner, whereas at 30 °C min^{-1} two nucleation centers appeared – one at 15 and the other at 52 min, assuming the clock face position. An abrupt freezing event, which occurred at around –30 °C in the cooling procedure, is documented in Video S1 and S2.

Note that the small dark rectangles that show throughout the background of the image (on as well as out of the frozen drop) in Fig. 10 and S21 are small ice crystals condensed from the air. These condensed water crystals are more pronounced and larger upon the 2 °C min^{-1} (Video S1 and S2) cooling compared to the higher rates, as a longer time for the crystal growth is allowed in the former case. In certain scenarios, these ice crystals condensed also on the droplet surface.

3.3.2. *Heating the samples*

The OCM images of the droplets of the CBSs (pH 4.0) at the warming rate of 2 °C min^{-1} are shown in Fig. 12 (to review all of the recorded images, see Video S3). Previously, the droplet was cooled at the rate of 2 °C min^{-1}. We can observe the dark inner part of the drop, the more translucent rim, and the ice crystals growing out from the edges of the frozen droplet. While the droplet was being heated, we did not detect any major changes until reaching T_{g2} (-40 °C) and slightly above. Only in the vicinity of T_{g1}, at around –33 °C, the darker inner region commenced to grow toward the perimeter of the droplet. We assign this expansion of the dark region to the devitrification of the FCS$_1$, followed by the crystallization. With further heating above −25 °C, the melting started to become prominent at −15 °C. As the heating continued, the whole droplet melted from the perimeter inwards. Note that the small crystals at a distance from the drop melt at 0 °C; the fact proves that these are ice crystals. The OCM images of the droplets, relating to all of the pH values and taken just before the melting ended, are provided in Figure S24 and S25. Some of the small ice crystals in the vicinity of the drop nevertheless melt at temperatures between −15 and −1 °C, probably due to the nanofilm that spreads from the drop (de Gennes 1985, Qazi et al. 2019, Vetráková et al. 2023). A similar scenario is observable in Video S3 and S4, applying to solutions at all of the examined pH values.

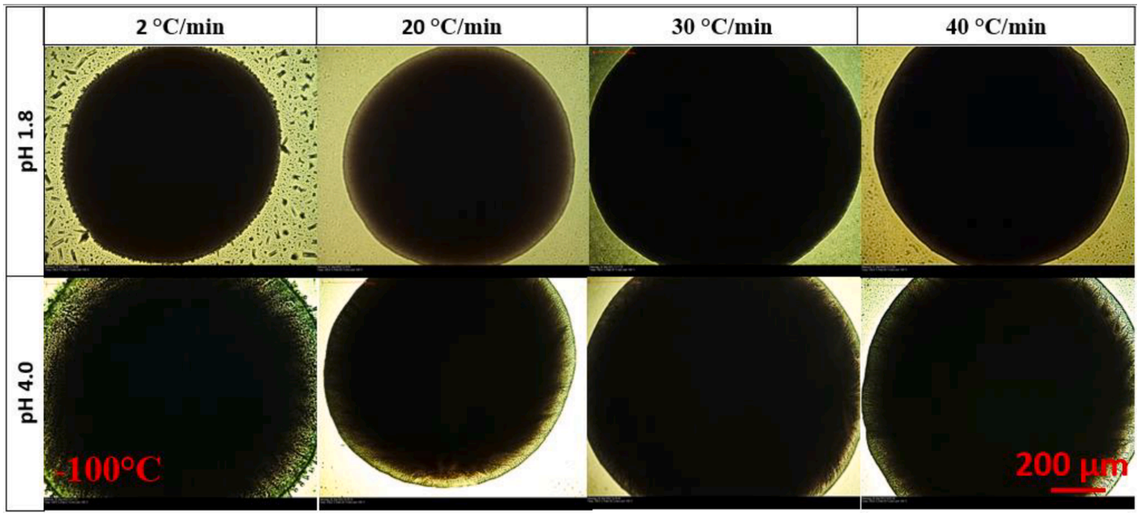

Fig. 10. The OCM images of the 0.6 M CBSs at the pH values 1.8 (1st row) and 4.0 (2nd row) at −100 °C after applying the cooling rates indicated in the header. The images were taken with unpolarized transmitted light. The scale of 200 μm is valid for all the pictures.

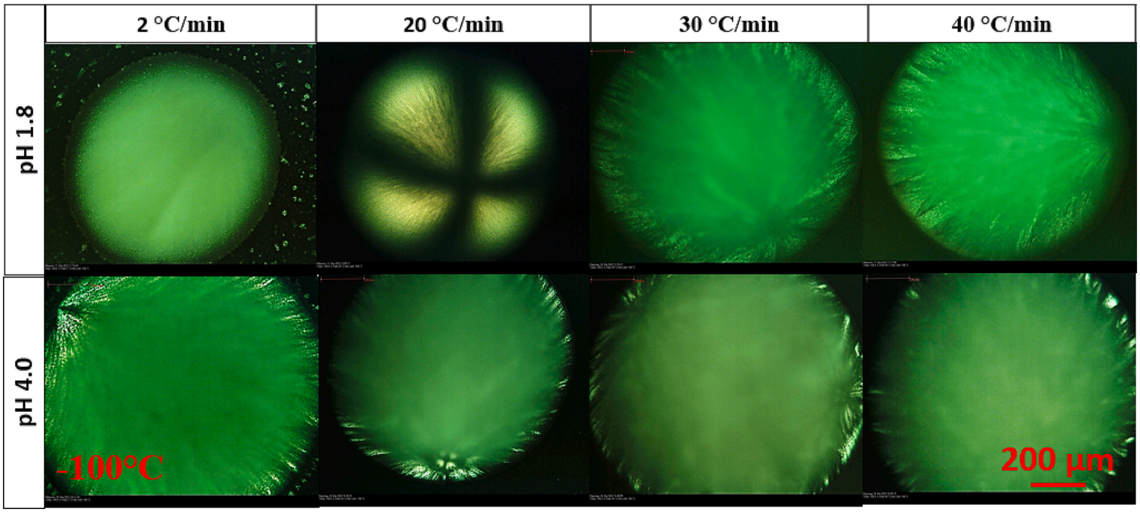

Fig. 11. The OCM images of the 0.6 M CBS at the pH values 1.8 (1st row) and 4.0 (2nd row) at −100 °C after applying various cooling rates. The images were taken with light transmitted through the polarization filters. The scale of 200 μm is valid for all the pictures.

4. Discussion

The acidity increase, having diverse intensities was induced by the freezing in all of the examined sodium citrate solutions. The observations are summarized in the results; here, we intend to propose explanations and draw practical implications for efficient freezing procedures. Citric acid has three acidic protons on the carboxylic groups, with $pKa_1 = 3.16$, $pKa_2 = 4.76$, $pKa_3 = 6.40$ (Apelblat 2014). The speciation diagram for citric acid and its three salts at various acidities is presented in Fig. 13.

We consider two major factors of influence on the acidity in FCSs: the freeze concentration effect and the fractional salt crystallization. The freeze concentration effect is caused by a gradual reduction in the volume of the solution, a process due to ice crystallization and growth. Mineral acids were previously found to freeze-concentrate by 3–4 orders of magnitude, as indicated by the enhanced protonation of CR (Heger et al. 2006). We assume that the freeze concentration effect embodies a major contributor to the acidity drop at the examined low pHs (below 3.5), where a monotonic decrease of acidity upon cooling the frozen solutions is observed (Fig. 6). At the pHs below 2.0, the freezing produces highly acidic environments with the H_{2-}^{frozen} lower than −1.0 (Figs. 7, S13 and S16). We did not examine these conditions in greater detail, as the buffering capacity is low at these pHs. In the buffer solutions that have the initial pHs between 2.5 and 4.5, the acidity increases only by less than 1.3 units, probably due to the buffering action of the citrate-monosodium-disodium system (Fig. 13). At the pH 3.0, the freezing-induced acidity increase does not depend on the buffer concentration in the range of 0.020 to 0.600 M (Fig. 8 and S20). These findings agree with the only previously reported acidity changes determination in the CBSs via UV–VIS indicators: Orii and Morita (1977) established by visual inspection a slight acidity increase in 0.15 M citrate at pH 3.1. Our results are, by extension, further supported through a mild acidity increase in the citrate at pH 4.0 immediately after the ice formation (Sundaramurthi and Suryanarayanan 2011) and at the pHs of 6.5–5.5 (by ca −0.5 at −10 °C) (Kolhe et al. 2010); both of the referenced research groups employed low temperature electrodes. The increase in acidity was observed also in lyophilized trehalose-citrate systems (Govindarajan et al. 2006a).

The other factor that influences the acidity lies in the crystallization of the buffer components; at all of the pHs, this effect was reliably identified via the DSC. The 3 °C min^{-1} cooling thermograms comprise peaks preceding the ice crystallization (Fig. 4), whereas in the 30 °C

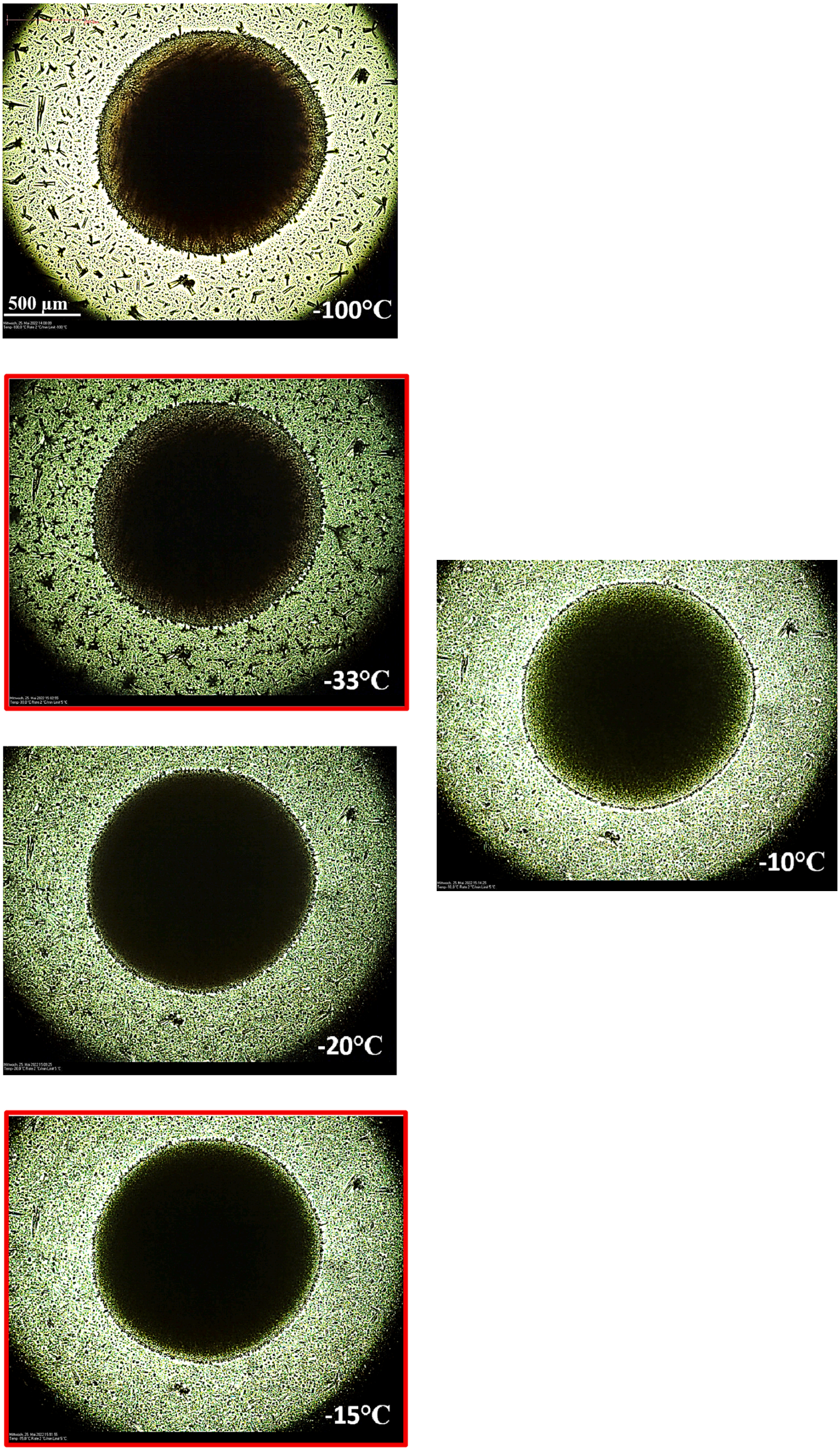

Fig. 12. The OCM images of the 0.6 M CBS for pH 4.0 at the various warming temperatures. The droplet was cooled down and heated up at 2 °C min^{-1}. The images were taken with unpolarized transmitted light (scale 500 μm). During the heating of the frozen droplet, no significant changes were observed at T_{g2} (-40 °C); only in the vicinity of T_{g1}, at around –33 °C, the darker inner region commenced to grow toward the perimeter of the droplet. With further heating above −25 °C, the melting started to become prominent at −15 °C. As the heating continued, the whole droplet melted from the perimeter inwards. This can be well observed in Video S3.

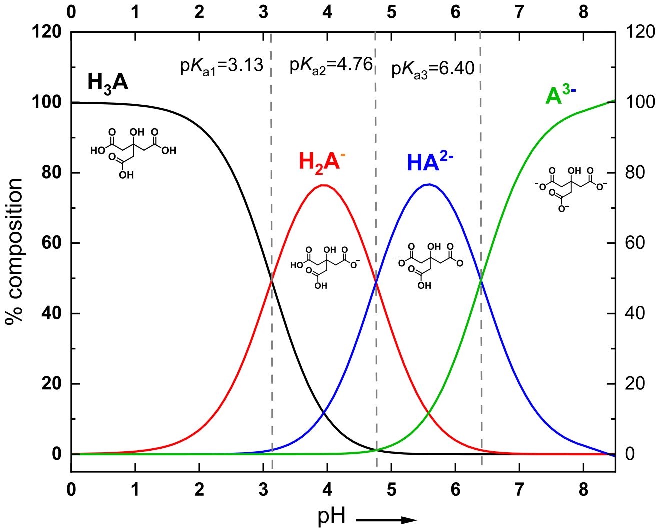

Fig. 13. The speciation diagram of citric acid. The calculations are detailed in the SI Text 1.

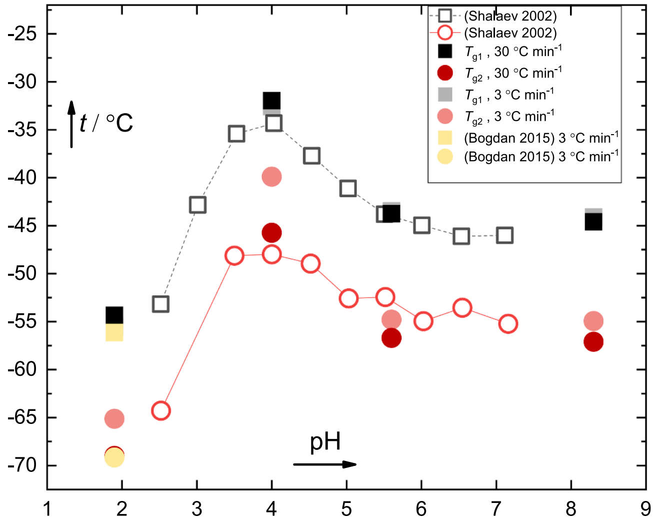

Fig. 14. The temperature dependence of the T_gs in the range of pHs as determined in the present study (full symbols) and as reported previously by Shalaev et al. (2002) (empty symbols), and Bogdan et al. (2014b) (light yellow). (For interpretation of the references to color in this figure legend, the reader is referred to the web version of this article.)

min^{-1} procedure the single exothermic peak is broader than the crystallization peak of the pure ice (Fig. 3). The crystallization peak at pH = 4.0 resembles that of the pure water, while those at the other pH show a larger tailing; in the latter case, the samples exhibited a more substantial acidity increase. Such results suggest that the FCS reaches the solubility limits, and, upon cooling, the solubility curve is followed. In the 3 °C min^{-1} cooling (Fig. 4), the buffer components started to precipitate at temperatures higher than those at which the ice did, but at the rate of 30 °C min^{-1} (Fig. 3) the buffer component precipitated together with the ice, presumably at the eutectic composition. The solubility of the citric acid at −0.15 °C was reported to be 1.89 M, dropping down to 0.066 M at the eutectic temperature of −13.15 °C (Dekruif et al. 1982). The precipitated sodium citrate monohydrate was identified in frozen solutions by X-ray diffraction (Sundaramurthi and Suryanarayanan 2011b).

The DSC thermograms reveal the liquid-to-glass transitions at temperatures below freezing. Apparently, not all of the solutes crystallized, a part of them remaining as a supercooled solution to vitrify at the lower temperatures, as indicated by the OCM (Figure S21). At each pH, we observed two glass transition temperatures (Fig. 5 and S10) varying by several degrees according to the cooling rate (Table S3); however, the changes in the isobaric heat capacities accompanying the glass-to-liquid transitions after either the 3° or the 30 °C min^{-1} cooling, depicted in Figure S27, accounted for less than 20 %. Such behavior is expected in good glass forming solutes, including citrate buffers, but contrasts with that of well-crystallizing salts (e.g., NaCl), whose vitrification was noticed at the cooling rate of 100 °C min^{-1} but not at the rates below 20 °C min^{-1} (Imrichova et al. 2019). The two glass transitions indicate the presence of two glasses, where the T_{g1} glass corresponds to that with the higher concentration of the citrate buffer (FCS_1) and the T_{g2} glass relates to that having the lower concentration (FCS_2). The dependence of the T_gs on the solutions' pH values agrees well with the dependence previously determined (Lu and Zografi 1997, Shalaev et al. 2002, Bogdan et al. 2014b) (Fig. 14). We also noticed that the relative amounts of the FCSs change with the cooling rates (Figure S27); this fact, together with the extent of the aggregation and buffer crystallization, is related to the size distribution in the ice crystals, which in turn influences the structures of the lyophilized particles (Vetráková et al. 2019, Fang et al. 2020, Vetráková et al. 2020, Závacká et al. 2022).

Upon further cooling, in the samples at the temperatures lower than −25 °C, the process is accompanied by only a slight increase in the acidity (Figs. 6, 7, 8, S20) at the pHs below 3.5. The smallest additional acidity changes in all of the pHs correspond to the smallest change in the heat capacity of the T_{g1}, measured at pH = 1.8; this may be interpreted such that only a minor portion of the FCS_1 eventually vitrifies (Fig. 6 and S27). The assumed scenario was positively confirmed through the OCM, where a higher quantity of the FCSs was detected at pH 4.0 than at pH 1.8 (Fig. 10). However, in the original acidities above pH 4.0, further cooling resulted in a decreased acidity (an increased H_{2-}^{frozen} value) as compared to −25 °C; the acidity then proceeded towards the initial solution's pH (Fig. 6). Thus, the cooling below −25 °C moderated the original stark freezing-induced acidity increase at these acidities. To illustrate this, let us note that in the solution with the initial pH 8.0 the freezing-induced acidity dropped to 5.7 but increased to 6.0 upon the glass transition (Fig. 6, dark green). The process is reversible, namely, the warming causes the solute to acidify via devitrification, dissolution, or dilution. To approach more closely the common industrial freezing procedure, we froze the solutions in the ethanol bath at −60 °C. The acidity changes connected to the warming process were observed also in the samples frozen at −60 °C (Figure S29).

By extension, the pH and the cooling conditions determine how the buffer concentration affects the pH change during the cooling. At pH ≥ 4.0, we notice that the increased buffer concentration results in a smaller acidity rise than the lower one (Figs. 8 and 9). We explain this behavior by the uncomplete crystallization of the sodium salts of the citric acid. In the cooling process, a simultaneous ice and sodium citrates' precipitation can produce a supersaturated eutectic mixture of a high viscosity, which has a low tendency to crystallize (Shalaev et al. 2002, Bogdan et al. 2014b). At the higher buffer concentrations, the crystallization is less complete, and therefore a high buffering capacity is preserved, leading to a less prominent freezing-induced acidity change. A similar phenomenon was observed also in Good's buffers, where 1 mM of the HEPES buffer solution showed a higher acidification upon freezing compared to 50 mM upon cooling at −196 °C (Vesely et al. 2021). The composition of the FCS influences the T_g. The T_gs exhibit almost identical values at the pHs of 8.3 and 5.6 (Table S3); we therefore expect the presence of similar compositions in the veins of the ice matrix. This fact can be explained by the precipitation of the trisodium citrate. The explanation is corroborated also by the fact that at pHs 5.0–8.0 a gradually larger acidity change occurs, corresponding to the increased amount of the crystallizable trisodium citrate in the original solution (Fig. 6, 7, and S16). The freezing of the CBSs at pH <4.0 always caused an acidity increase, with lower H_{2-}^{frozen} values; this is the region where the CBSs exhibit the highest buffering capacity, as can be deduced from the speciation diagram (Fig. 13). The observed concentration dependence of the CBSs stands in contrast to the behavior of the sodium phosphate buffer, where the acidity decreased from the original pH 7.5 to the H_{2-}^{frozen} of 1.4 in the 50 mM and 6.1 in the 1 mM buffers (Krausková et al. 2016). The explanation can lie in that the 50 mM phosphate salts precipitate, whereas the citrate salts vitrify, at least in part.

The study of the cooling rates (Fig. 7) and concentration dependences (Figs. 8 and 9) confirms the acidification mechanism: The slow cooling allows the citrate salts to crystallize more extensively, inducing a slightly larger acidification. We tested this premise and cooled the samples in the liquid methane at −196 °C. Generally, this medium is known to provide cooling rates faster by an order of magnitude than those achievable with liquid nitrogen. The fast-cooling rate produced a less acidic frozen solution in the 0.6 M buffer solutions than the slower cooling (Figures S20, S28). Such a scenario, however, does not apply to the 50 mM solutions, in which the freezing procedure employed does not significantly impact the H_{2-}^{frozen} values (Fig. 7 and Figure S16).

Furthermore, we attempted to design an optimal buffer concentration for each pH; the results of this process are shown in Fig. 9. The negligible acidity increase (<0.1) was obtained via freezing the 0.6 M buffer at pHs 4 and 5 and the 1.3 M solutions at pHs 6 and 7. Fig. 9 also exposes the large acidity increases in the low concentration buffers. In the highly concentrated solutions, the crystallization is incomplete, and the buffering capacity stabilizes the pH.

Regarding the procedural methodology, the OCM delivers morphology-bound information. The less concentrated FCS_2, having lower glass-to-liquid transition temperatures, were not resolved during the heating in the micrograms. The FCS_2 should be separated from the directional growth of the dendritic ice (Bogdan et al. 2014a, b); such a distinction was not feasible in the random ice nucleation within our experiments. However, the FCS_1 was well discernible by means of the glass-to-liquid transition, which occurs in the heating processes at around the T_{g1} temperatures and is specific for each pH, with, for instance, pH = 4.0 at −33 °C (Video S3) and pH = 5.6 at −40 °C (Video S4). In the vicinity of these temperatures, the acidity changes were also noticed (Fig. 6).

Upon the heating, the melting endotherms of the citrate buffer components were never identified separately from the ice melting endotherm in the DSC thermograms. This finding stands in contrast with the behavior of the $NaCl{\cdot}2H_2O$ (Imrichova et al. 2019) and embodies the probable explanation of why the citrate buffer was considered not to crystallize during the freezing (Shalaev et al. 2002). The relevant article by Shalaev et al. (2002) presented only those heating thermograms where the citrate buffer components' crystallization endotherms are not discerned. The data outlined in our study (the freezing-induced acidity jump, peaks in the DSC cooling scans, and low melting temperatures, for instance) clearly indicate that, besides the glass formation, a portion of the citrate buffer crystallizes.

4.1. Implications for the freezing and storage

This article shows, among other aspects, that freezing a 50 mM citrate buffer at pH 7.0 down to −25 °C produces the acidity of 4.9 (Fig. 6). Such a freezing-induced acidity increase can significantly reduce the antibacterial activity of penicillin (Symington et al. 2012), possibly affecting other processes too. The proposed results open a path towards taking practical steps to minimize the harm to the frozen samples. Thus, as can be inferred from Fig. 6, if the 50 mM buffer solution is kept in the frozen state, the temperatures of −25 °C and −60 °C are recommended for pHs < 3.5 and <4.0, respectively.

The freezing temperature does not influence the final acidity in an excessively significant manner. However, a trend is notable especially in samples whose initial pH values range above 4.0 (Fig. 7): The fast cooling results in a smaller acidity change compared to the gradual cooling. Consequently, if choice is available, fast cooling in liquid nitrogen or even in an ethanol bath at −80 °C should be preferred over the slower cooling procedures. Most importantly, the experiments suggest a key impact of the buffer concentration on the resulting acidity in the frozen state. In this context, Fig. 9 provides valuable advice on how to apply the optimal buffer concentration at the demanded pH. The citrate buffer seems to be well usable at pHs 3 to 7; otherwise, the buffers suffer from an acidity increased by more than 1.5 units, unless a high concentration and the fast cooling are employed (Figs. 6, 7, S13 to S19). Concerning the storage temperature, no acidity changes were observed below the T_{g2} (an unexplained exception is the case of pH = 4, Fig. 6). Thus, the pH-dependent T_{g2} can provide the guidelines for the highest conceivable storage temperatures (Fig. 14) in the frozen samples. The mild acidification accompanying the glass-to-liquid transition rationalizes thawing the citrate buffers in the fastest possible way. This is generally recommended, as such a process also minimizes the recrystallization (Cao et al. 2003).

5. Conclusions

The article presents evidence for the freezing-induced acidity increase in CBSs, relating this effect to the concentration, pH of the initial solution, temperature, and cooling rate. The methods and instruments, namely, DSC, OCM, and acid-base indicator, deliver complementary information that allows representing in full the processes in the freezing steps and during the cooling, both being pre-lyophilization stages. By cooling the CBSs (pH < 4), the ice and the buffer components crystallize due to the reduced solubility; this phase is typically accompanied by an acidity increase. Upon further cooling, the acidified FCSs concentrate more extensively and increase their viscosity, inducing small acidity changes before the eventual vitrification. The glasses do not show substantial acidity variations when cooled down again. At heating, the glass-to-liquid transition is followed by an additional acidity change, a possible by-effect of the resumed crystallization. A subsequent heating leads to the eutectic melting and also the dilution of the FCSs. The initial concentration of the buffers is selectable to minimize the freezing-induced acidity changes.

CRediT authorship contribution statement

Behera Susrisweta: Investigation, Data curation, Writing – original draft, Visualization, Writing – review & editing. **Lukáš Veselý:** Visualization, Data curation, Writing – review & editing. **Radim Štůsek:** Visualization, Data curation, Writing – review & editing. **Astrid Hauptmann:** Supervision, Visualization. **Thomas Loerting:** Supervision, Visualization, Data curation. **Dominik Heger:** Conceptualization, Resources, Writing – review & editing, Supervision, Funding acquisition.

Declaration of Competing Interest

The authors declare the following financial interests/personal relationships which may be considered as potential competing interests: Behera Susrisweta reports financial support and travel were provided by Central European Exchange Program for University Studies.

Data availability

Data will be made available on request.

Acknowledgement

The research was supported by Internal grant agency MU via project CZ.02.2.69/0.0/0.0/19_073/0016943 (MUNI/IGA/0991/2021) and by CEEPUS grant M - SI-1312-2122-150432 in the frame of the network “Water – a common but anomalous substance that has to be taught and studied”.

Appendix A. Supplementary data

Supplementary data to this article can be found online at https://doi.org/10.1016/j.ijpharm.2023.123211.

References

Abbatt, J.P.D., Nowak, J.B., 1997. Heterogeneous interactions of HBr and HOCl with cold sulfuric acid solutions: Implications for arctic boundary layer bromine chemistry. J. Phys. Chem. A 101 (11), 2131–2137.

Alkhamis, K.A., 2009. Influence of Solid-State Acidity on the Decomposition of Sucrose in Amorphous Systems II (Effect of Buffer). Drug Dev. Ind. Pharm. 35 (4), 408–416.

Apelblat, A., 2014. Citric Acid. Springer Cham.

Authelin, J.R., Rodrigues, M.A., Tchessalov, S., Singh, S.K., McCoy, T., Wang, S., Shalaev, E., 2020. Freezing of Biologicals Revisited: Scale, Stability, Excipients, and Degradation Stresses. J Pharm Sci 109 (1), 44–61.

Badawy, S.I.F., Hussain, M.A., 2007. Microenvironmental pH modulation in solid dosage forms. J. Pharm. Sci. 96 (5), 948–959.

Bartels-Rausch, T., Jacobi, H.W., Kahan, T.F., Thomas, J.L., Thomson, E.S., Abbatt, J.P. D., Ammann, M., Blackford, J.R., Bluhm, H., Boxe, C., Domine, F., Frey, M.M., Gladich, I., Guzmán, M.I., Heger, D., Huthwelker, T., Klán, P., Kuhs, W.F., Kuo, M.H., Maus, S., Moussa, S.G., McNeill, V.F., Newberg, J.T., Pettersson, J.B.C., Roeselová, M., Sodeau, J.R., 2014. A review of air–ice chemical and physical interactions (AICI): liquids, quasi-liquids, and solids in snow. Atmos. Chem. Phys. 14 (3), 1587–1633.

Berg, L.V.D., 1961. Changes in pH of Milk During Freezing and Frozen Storage1. J. Dairy Sci. 44 (1), 26–31.

Bogdan, A., Molina, M.J., 2017. Physical Chemistry of the Freezing Process of Atmospheric Aqueous Drops. Chem. A Eur. J. 121 (16), 3109–3116.

Bogdan, A., Molina, M.J., Tenhu, H., Bertel, E., Bogdan, N., Loerting, T., 2014a. Visualization of Freezing Process in situ upon Cooling and Warming of Aqueous Solutions. Sci. Rep. 4, 7414.

Bogdan, A., Molina, M.J., Tenhu, H., Loerting, T., 2014b. Multiple Glass Transitions and Freezing Events of Aqueous Citric Acid. Chem. A Eur. J. 119 (19), 4515–4523.

Bogdan, A., Molina, M.J., Tenhu, H., 2016. Freezing and glass transitions upon cooling and warming and ice/freeze-concentration-solution morphology of emulsified aqueous citric acid. Eur. J. Pharm. Biopharm. 109, 49–60.

Caillet, A., Puel, F., Fevotte, G., 2006. In-line monitoring of partial and overall solid concentration during solvent-mediated phase transition using Raman spectroscopy. Int. J. Pharm. 307 (2), 201–208.

Cao, E.H., Chen, Y.H., Cui, Z.F., Foster, P.R., 2003. Effect of freezing and thawing rates on denaturation of proteins in aqueous solutions. Biotechnol. Bioeng. 82 (6), 684–690.

Cavatur, R.K., Suryanarayanan, R., 1998. Characterization of Frozen Aqueous Solutions by Low Temperature X-ray Powder Diffractometry. Pharm. Res. 15 (2), 194–199.

Chang, B.R.C., 1992. Use of subambient thermal analysis to optimize protein lyophilization. Cryobiology 29, 632–656.

Chang, P., Chen, Z., Zhang, Y., Liu, Y., 2020. Direct measurement of aerosol pH in individual malonic acid and citric acid droplets under different relative humidity conditions via Raman spectroscopy. Chemosphere 241, 124960.

Chatre, C., Emmelin, C., Urbaniak, S., George, C., Cogné, C., 2019. Phase Transformations of Liquid Drops Containing Mineral Dust and Organic Compound (Citric Acid). Cryst. Growth Des. 19 (8), 4619–4624.

Chatterjee, K., Shalaev, E.Y., Suryanarayanan, R., Govindarajan, R., 2008. Correlation between chemical reactivity and the Hammett acidity function in amorphous solids using inversion of sucrose as a model reaction. J. Pharm. Sci. 97 (1), 274–286.

Daneshfar, A., Baghlani, M., Sarabi, R., Sahraei, R., Abbasi, S., Kaviyan, H., Khezeli, T., 2011. Solubility of citric, malonic, and malic acids in different solvents from 303.2 to 333.2 K. Energy Fuels 313.

de Gennes, P.G., 1985. Wetting: statics and dynamics. Rev. Mod. Phys. 57 (3), 827–863.

Dekruif, C.G., Vanmiltenburg, J.C., Sprenkels, A.J.J., Stevens, G., Degraaf, W., Dewit, H. G.M., 1982. Thermodynamic Properties of Citric-Acid and the System Citric-Acid Water. Thermochim Acta 58 (3), 341–354.

Fang, R., Bogner, R.H., Nail, S.L., Pikal, M.J., 2020. Stability of Freeze-Dried Protein Formulations: Contributions of Ice Nucleation Temperature and Residence Time in the Freeze-Concentrate. J Pharm Sci 109 (6), 1896–1904.

Govindarajan, R., Chatterjee, K., Gatlin, L., Suryanarayanan, R., Shalaev, E.Y., 2006a. Impact of freeze-drying on ionization of sulfonephthalein probe molecules in trehalose-citrate systems. J. Pharm. Sci. 95 (7), 1498–1510.

Govindarajan, R., Zinchuk, A., Hancock, B., Shalaev, E., Suryanarayanan, R., 2006b. Ionization states in the microenvironment of solid dosage forms: Effect of formulation variables and processing. Pharm. Res. 23 (10), 2454–2468.

Govindarajan, R., Landis, M., Hancock, B., Gatlin, L.A., Suryanarayanan, R., Shalaev, E. Y., 2014. Surface Acidity and Solid-State Compatibility of Excipients with an Acid-Sensitive API: Case Study of Atorvastatin Calcium. AAPS PharmSciTech 16 (2), 354–363.

Hauptmann, A., Podgoršek, K., Kuzman, D., Srčič, S., Hoelzl, G., Loerting, T., 2018. Impact of Buffer, Protein Concentration and Sucrose Addition on the Aggregation and Particle Formation during Freezing and Thawing. Pharm. Res. 35 (5).

Hauptmann, A., Hoelzl, G., Loerting, T., 2019. Distribution of Protein Content and Number of Aggregates in Monoclonal Antibody Formulation After Large-Scale Freezing. AAPS PharmSciTech 20 (2), 72.

Hauptmann, A., Hoelzl, G., Loerting, T., 2021. Optical cryomicroscopy and differential scanning calorimetry of buffer solutions containing cryoprotectants. Eur J Pharm Biopharm 163, 127–140.

Heger, D., Jirkovsky, J., Klan, P., 2005. Aggregation of methylene blue in frozen aqueous solutions studied by absorption spectroscopy. J. Phys. Chem. A 109 (30), 6702–6709.

Heger, D., Klanova, J., Klan, P., 2006. Enhanced protonation of cresol red in acidic aqueous solutions caused by freezing. J. Phys. Chem. B 110 (3), 1277–1287.

Heger, D., Govindarajan, R., Lu, E., Ewing, S., Lay-Fortenbery, A., Yuan, X., Veselý, L., Munson, E., Gatlin, L., Hancock, B., Suryanarayanan, R., Shalaev, E., 2023. Beyond pH: Acid/Base Relationships in Frozen and Freeze-Dried Pharmaceuticals. In: Principles and Practices of Lyophilization in Product Development and Manufacturing. F. Jameel. Springer International Publishing:, Cham, pp. 39–61.

Hemminger, W., Höhne, G., 1979. Grundlagen der Kalorimetrie. Verlag Chemie.

Imrichova, K., Vesely, L., Gasser, T.M., Loerting, T., Nedela, V., Heger, D., 2019. Vitrification and increase of basicity in between ice Ih crystals in rapidly frozen dilute NaCl aqueous solutions. J Chem Phys 151 (1), 014503.

Izutsu, K., Kadoya, S., Yomota, C., Kawanishi, T., Yonemochi, E., Terada, K., 2009. Freeze-drying of proteins in glass solids formed by basic amino acids and dicarboxylic acids. Chem Pharm Bull (Tokyo) 57 (1), 43–48.

Jung, J., Kawamura, K., 2011. Enhanced concentrations of citric acid in spring aerosols collected at the Gosan background site in East Asia. Atmos. Environ. 45 (30), 5266–5272.

Kadoya, S., Izutsu, K.-I., Yonemochi, E., Terada, K., Yomota, C., Kawanishi, T., 2008. Glass-State Amorphous Salt Solids Formed by Freeze-Drying of Amines and Hydroxy Carboxylic Acids: Effect of Hydrogen-Bonding and Electrostatic Interactions. Chem. Pharm. Bull. 56 (6), 821–826.

Kasper, J.C., Friess, W., 2011. The freezing step in lyophilization: Physico-chemical fundamentals, freezing methods and consequences on process performance and quality attributes of biopharmaceuticals. Eur. J. Pharm. Biopharm. 78 (2), 248–263.

Kets, E.P.W., Ijpelaar, P.J., Hoekstra, F.A., Vromans, H., 2004. Citrate increases glass transition temperature of vitrified sucrose preparations. Cryobiology 48 (1), 46–54.

Kheirolomoom, A., Kazemi-Vaysari, A., Ardjmand, M., Baradar-Khoshfetrat, A., 1999. The combined effects of pH and temperature on penicillin G decomposition and its stability modeling. Process Biochem. 35 (1), 205–211.

Kolhe, P., Amend, E., Singh, S.K., 2010. Impact of Freezing on pH of Buffered Solutions and Consequences for Monoclonal Antibody Aggregation. Biotechnol. Prog. 26 (3), 727–733.

Krausko, J., Runštuk, J., Nedĕla, V., Klán, P., Heger, D., 2014. Observation of a Brine Layer on an Ice Surface with an Environmental Scanning Electron Microscope at Higher Pressures and Temperatures. Langmuir 30 (19), 5441–5447.

Krausková, L., Procházková, J., Klašková, M., Filipová, L., Chaloupková, R., Malý, S., Damborský, J., Heger, D., 2016. Suppression of protein inactivation during freezing by minimizing pH changes using ionic cryoprotectants. Int. J. Pharm. 509 (1–2), 41–49.

Laird, T. (1997). “Ullmann’s Encyclopedia of Industrial Chemistry, 5th Edition VCH: Weinheim, Germany. 1996/1997. Section A, 28 vols. Section B, 8 vols. DM 19 400.” Organic Process Research & Development **1**(5): 391-392.

Li, M., Koranne, S., Fang, R., Lu, X., Williams, D.M., Munson, E.J., Bhambhani, A., Su, Y., 2021. Probing Microenvironmental Acidity in Lyophilized Protein and Vaccine Formulations Using Solid-state NMR Spectroscopy. J. Pharm. Sci. 110 (3), 1292–1301.

Literak, J., Klan, P., Heger, D., Loupy, A., 2003. Photochemistry of alkyl aryl ketones on alumina, silica-gel and water ice surfaces. Journal of Photochemistry and Photobiology a-Chemistry 154 (2–3), 155–159.

Lu, Q., Zografi, G., 1997. Properties of Citric Acid at the Glass Transition. J. Pharm. Sci. 86 (12), 1374–1378.

Lu, Q., Zografi, G., 1998. Phase behavior of binary and ternary amorphous mixtures containing indomethacin, citric acid, and PVP. Pharm Res 15 (8), 1202–1206.

Maltini, E., Anese, M., Shtylla, I., 1997. State diagrams of some organic acid-water systems of interest in food. CryoLetters 18, 263–268.

Murase, N., Franks, F., 1989. Salt Precipitation During the Freeze-Concentration of Phosphate Buffer Solutions. Biophys. Chem. 34 (3), 293–300.

Nangare, S., Vispute, Y., Tade, R., Dugam, S., Patil, P., 2021. Pharmaceutical applications of citric acid. Future Journal of Pharmaceutical Sciences 7 (1), 54.

Orii, Y., Morita, M., 1977. Measurement of pH of Frozen Buffer Solutions by Using pH Indicators. J. Biochem. 81 (1), 163–168.

Pudipeddi, M., Zannou, E.A., Vasanthavada, M., Dontabhaktuni, A., Royce, A.E., Josh, Y. M., Serajuddin, A.T.M., 2008. Measurement of surface pH of pharmaceutical solids: A critical evaluation of indicator dye-sorption method and its comparison with slurry pH method. J. Pharm. Sci. 97 (5), 1831–1842.

Qazi, M. J., H. Salim, C. A. W. Doorman, E. Jambon-Puillet and N. Shahidzadeh (2019). “Salt creeping as a self-amplifying crystallization process.” Science advances **5**(12): eaax1853-eaax1853.

Schoenmaker, L., Witzigmann, D., Kulkarni, J.A., Verbeke, R., Kersten, G., Jiskoot, W., Crommelin, D.J.A., 2021. mRNA-lipid nanoparticle COVID-19 vaccines: Structure and stability. Int. J. Pharm. 601, 120586.

Seema Thakral, J.S., Munjal, B., Suryanarayanan, R., 2021. Stabilizers and their interaction with formulation components in frozen and freeze-dried protein formulations. Adv. Drug Deliv. Rev. 173, 1–19.

Shalaev, E.Y., Gatlin, L.A., 2005. The Impact of Buffer on Solid-State Properties and Stability of Freeze-Dried Dosage Forms. Formulation and Process Development Strategies for Manufacturing Biopharmaceuticals 507–519.

Shalaev, E.Y., Johnson-Elton, T.D., Chang, L.Q., Pikal, M.J., 2002. Thermophysical properties of pharmaceutically compatible buffers at sub-zero temperatures: Implications for freeze-drying. Pharm. Res. 19 (2), 195–201.

Summers, M.P., Enever, R.P., 1976. Preparation and properties of solid dispersion system containing citric acid and primidone. J Pharm Sci 65 (11), 1613–1617.

Sundaramurthi, P., Shalaev, E., Suryanarayanan, R., 2010. Calorimetric and Diffractometric Evidence for the Sequential Crystallization of Buffer Components and the Consequential pH Swing in Frozen Solutions. J. Phys. Chem. B 114 (14), 4915–4923.

Sundaramurthi, P., Suryanarayanan, R., 2011a. Predicting the crystallization propensity of carboxylic acid buffers in frozen systems–relevance to freeze-drying. J Pharm Sci 100 (4), 1288–1293.

Sundaramurthi, P., Suryanarayanan, R., 2011b. Thermophysical properties of carboxylic and amino acid buffers at subzero temperatures: relevance to frozen state stabilization. J Phys Chem B 115 (21), 7154–7164.

Symington, A., Leow, L.M., Griffiths, P.T., Cox, R.A., 2012. Adsorption and Hydrolysis of Alcohols and Carbonyls on Ice at Temperatures of the Upper Troposphere. J. Phys. Chem. A 116 (24), 5990–6002.

Takenaka, N., Tanaka, M., Okitsu, K., Bandow, H., 2006. Rise in the pH of an unfrozen solution in ice due to the presence of NaCl and promotion of decomposition of gallic acids owing to a change in the pH. J. Phys. Chem. A 110 (36), 10628–10632.

Thomas, L.V., Nair, P.D., 2011. (Citric acid-co-polycaprolactone triol) polyester: a biodegradable elastomer for soft tissue engineering. Biomatter 1 (1), 81–90.

Thorat, A.A., Suryanarayanan, R., 2019. Characterization of Phosphate Buffered Saline (PBS) in Frozen State and after Freeze-Drying. Pharm Res 36 (7), 98.

Timko, R.J., Lordi, N.G., 1979. Thermal characterization of citric acid solid dispersions with benzoic acid and phenobarbital. J Pharm Sci 68 (5), 601–605.

Trissel, L. A. T. L. A. A. M. C. H. D. P. H. K. N. A. S. o. H.-S. P. (1996). Handbook on injectable drugs. [Bethesda Md.], ASHP.

Ueda, M., Hirokawa, N., Harano, Y., Moritoki, M., Ohgaki, K., 1995. Change in microstructure of an aqueous citric acid solution under crystallization. J. Cryst. Growth 156 (3), 261–266.

Van den Berg, L., 1966. PH CHANGES IN BUFFERS AND FOODS DURING FREEZING AND SUBSEQUENT STORAGE. Cryobiology 3 (3), 236–1000.

Van den Berg, L., Rose, D., 1959. Effect of Freezing on the pH and Composition of Sodium and Potassium Phosphate Solutions - the Reciprocal System KH_2PO_4 - Na_2HPO_4 - H_2O. Arch. Biochem. Biophys. 81 (2), 319–329.

Vesely, L., Susrisweta, B., Heger, D., 2021. Making good's buffers good for freezing: The acidity changes and their elimination via mixing with sodium phosphate. Int J Pharm 593, 120128.

Vetráková, Ľ., Vykoukal, V., Heger, D., 2017. Comparing the acidities of aqueous, frozen, and freeze-dried phosphate buffers: Is there a "pH memory" effect? Int. J. Pharm. 530 (1–2), 316–325.

Vetráková, Ľ., Neděla, V., Runštuk, J., Heger, D., 2019. The morphology of ice and liquid brine in an environmental scanning electron microscope: a study of the freezing methods. Cryosphere 13 (9), 2385–2405.

Vetráková, Ľ., Neděla, V., Runštuk, J., Tihlaříková, E., Heger, D., Shalaev, E., 2020. Dynamical in-situ observation of the lyophilization and vacuum-drying processes of a model biopharmaceutical system by an environmental scanning electron microscope. Int. J. Pharm. 585, 119448.

Vetráková, L., Neděla, V., Závacká, K., Yang, X., Heger, D., 2023. Technical note: Sublimation of frozen CsCl solutions in an environmental scanning electron microscope (ESEM) – determining the number and size of salt particles relevant to sea salt aerosols. Atmos. Chem. Phys. 23 (7), 4463–4488.

Vijayarajkumar, P. C., R. K.; Narne, R (2012). "Efavirenz Loaded Novel Citric Acid Dendritic Architecture for Increased Solubility and Sustained Delivery." J. Pharm. Drug. Delivery Res.: 1-5.

Waterman, K.C., Adami, R.C., Alsante, K.M., Antipas, A.S., Arenson, D.R., Carrier, R., Hong, J., Landis, M.S., Lombardo, F., Shah, J.C., Shalaev, E., Smith, S.W., Wang, H., 2002. Hydrolysis in pharmaceutical formulations. Pharm Dev Technol 7 (2), 113–146.

Webb, S.D., Webb, J., Hughes, T., Sesin, D., Kincaid, A., 2002. Freezing bulk-scale biopharmaceuticals using common techniques - and the magnitude of freeze-concentration. BioPharm 15, 22-+.

Workman, E.J., Reynolds, S.E., 1950. Electrical Phenomena Occurring during the Freezing of Dilute Aqueous Solutions and Their Possible Relationship to Thunderstorm Electricity. Phys. Rev. 78 (3), 254.

Wouters, O.J., Shadlen, K.C., Salcher-Konrad, M., Pollard, A.J., Larson, H.J., Teerawattananon, Y., Jit, M., 2021. Challenges in ensuring global access to COVID-19 vaccines: production, affordability, allocation, and deployment. Lancet 397 (10278), 1023–1034.

Wu, C., Shamblin, S., Varshney, D., Shalaev, E., 2015. Advance Understanding of Buffer Behavior during Lyophilization. Lyophilized Bilogics and Vaccines, Modality-Based Approaches, pp. 25–41.

Yang, J., Webb, A.R., Ameer, G.A., 2004. Novel Citric Acid-Based Biodegradable Elastomers for Tissue Engineering. Adv. Mater. 16 (6), 511–516.

Yi Yao, M.-H.-W., Zhao, K.-Y., Wang, C.-C., 1998. Assay for enzyme activity by following the absorbance change of pH-indicators. J. Biochem. Bioph. Methods 36 (2–3), 119–130.

Závacká, K., Neděla, V., Tihlaříková, E., Šabacká, P., Maxa, J., Heger, D., 2021. ESEM Methodology for the Study of Ice Samples at Environmentally Relevant Subzero Temperatures: "Subzero ESEM". Microsc. Microanal. 1–14.

Závacká, K., Neděla, V., Olbert, M., Tihlaříková, E., Vetráková, Ľ., Yang, X., Heger, D., 2022. Temperature and Concentration Affect Particle Size Upon Sublimation of Saline Ice: Implications for Sea Salt Aerosol Production in Polar Regions. Geophys. Res. Lett. 49 (8).